Rainfall Estimation from ESMR-5 Measurements and Application to El Niño

HYO-SUK LIM*

Department of Meteorology, Texas A&M University, College Station, Texas

C. E. GRAVES

Department of Earth and Atmospheric Sciences, Saint Louis University, St. Louis, Missouri

G. R. NORTH AND T. T. WILHEIT

Climate System Research Program, Department of Meteorology, Texas A&M University, College Station, Texas

(Manuscript received 10 January 1994, in final form 1 June 1994)

ABSTRACT

An algorithm to estimate monthly 5° × 5° area-averaged rain rate over the oceans from January 1973 to December 1976 using single-channel microwave data from the *Nimbus-5* satellite has been developed. This study extends the work of Shin et al. by including the full width of scan angles (from −50° to 50°) in order to reduce sampling error. The scan-angle dependence of the estimated rain rate due to variable antenna sidelobe effects, surface emissivity, and propagation pathlength is eliminated using a statistical method. A globally uniform beam-filling correction factor of 2.2 is applied in this study. Comparison with island station rainfall measurements over the Pacific shows a remarkably high correlation between two data in the equatorial dry zone and South Pacific convergence zone (SPCZ) but a low correlation in the extratropics and equatorial western Pacific. It is also proved that the retrieved rain rates are statistically significant.

The rainfall deviations from non–El Niño years April 1973 to December 1975 reveal the temporal and spatial variations produced by the 1972–73 and 1976–77 El Niño episodes. We observe an increase of rainfall over the eastern and central equatorial Pacific Ocean and a decrease over the equatorial western Pacific Ocean and eastern Australia during these events. Consistent with previous work, the rainfall anomaly of the 1972–73 El Niño was much stronger than that of the 1976–77 El Niño.

1. Introduction

Precipitation plays an important part in all aspects of life on our planet. Likewise, rainfall is crucial in determining the role of latent heating in the energy budget of the atmosphere and climate system. In spite of its importance, precipitation is one of the most difficult elements of weather to measure. In the last decade, various satellite techniques have been developed to gather global precipitation data. Most retrieval methods are based on visible, infrared, or microwave radiation. Unlike visible and infrared radiation, microwave radiation can penetrate clouds, especially at the low-frequency end of the spectrum. Hydrometeors can directly modify the terrestrial microwave emission. Thus, spaceborne microwave radiometers can more directly estimate precipitation. Because of this fact, many studies have been undertaken to measure precipitation using remotely sensed microwave measurements.

The first quantitative attempt to relate rainfall to microwave emissions was by Wilheit et al. (1977). The model assumed the M–P (Marshall and Palmer 1948) raindrop size distribution from the surface to the freezing level. An additional 0.5 km of nonprecipitating cloud (with a concentration of 0.5 g m^{-3}) was assumed just beneath the freezing level. A temperature lapse rate of 6.5°C km^{-1} and 80% relative humidity at the surface were assumed and the relative humidity was assumed to increase linearly with height to 100% at the freezing level and above. Therefore, the freezing level serves as a proxy variable for both the rain-layer thickness and for the atmospheric water vapor content. They quantified the relationship between microwave radiance data at 19.35 GHz (1.55 cm) and rain intensity over the oceans. The relationship between rain rate and brightness temperature for 19.35 GHz (R–T relationship) was calculated for the five freezing levels 1, 2, 3, 4, and 5 km.

Seasonal precipitation frequencies for the tropical oceans from the *Nimbus-5* Electrical Scanning Micro-

* Current affiliation: Universities Space Research Association, NASA/GSFC, Greenbelt, Maryland.

Corresponding author address: Dr. Gerald R. North, Climate System Research Program, Department of Meteorology, Texas A&M University, College Station, TX 77843-3150.

wave Radiometer (ESMR-5) data were calculated by Kidder and Vonder Haar (1977). Zonal mean freezing levels for the season (Oort and Rasmusson 1971; Taljaard et al. 1969) were cojoined with the R–T relationship from Wilheit et al. (1977) to yield zonal threshold brightness temperatures for the detection of seasonal oceanic precipitation. Rao et al. (1976) made a global atlas of rain rate over the oceans using ESMR-5 data for 1973 and 1974. Rain rate was calculated primarily using the R–T relationship from Wilheit et al. (1975). They used a climatological freezing level. Shin et al. (1990), using the R–T relationship of Wilheit et al. (1977), developed a rainfall retrieval algorithm over tropical oceans based on brightness temperature histograms in each 5° × 5° grid box for each season. Kummerow and Weinman (1988) developed the relationships between brightness temperature for 37 GHz and rain rate from horizontally finite precipitating clouds that contain both ice and liquid hydrometeors. It was found that precipitating ice at the top of the cloud depresses the brightness temperatures considerably, especially for heavier rain rates where the importance of scattering relative to absorption and emission increases dramatically.

Single-channel retrievals are limited by the variability of surface emissivity, atmospheric water vapor, surface wind, and nonraining cloud liquid water content. To overcome these limitations, a host of multichannel techniques have been developed. Smith and Mugnai (1988) investigated the impact of time-dependent cloud microphysical structure on the radiative transfer to space at multiple microwave frequencies centered 19.35, 22.235, 37.0, 89.5, 100.0, 130.0, and 231.0 GHz. Results show that prior to or during the precipitation process, the cloud liquid water within developed cumulus can have a dominant effect on the microwave signal observed above the cloud. As a result the relation between microwave brightness temperature and rain rate is dramatically altered by cloud water. A monthly rainfall retrieval algorithm over the oceans from histograms of Special Sensor Microwave/Imager (SSM/I) brightness temperatures has been designed by Wilheit et al. (1991). The impact of water vapor variability is reduced by a linear combination of the 19.35 and 22.235 GHz. From the histograms of brightness temperatures collected over a month for a 5° × 5° grid box, parameters of the lognormality in the rain-rate distributions are estimated. The monthly rainfall over the 5° × 5° grid box is computed directly from these parameters. Freezing level was calculated from the 19.35- and 22.235-GHz brightness temperature histograms.

The brightness temperatures for the ESMR-5 instrument have a scan-angle bias due to variable antenna sidelobe effects in addition to the surface emissivity and atmospheric propagation pathlength. A linear empirical correction that depends only on scan position was applied to the data by the National Aeronautics and Space Administration (NASA) instrument team. In spite of this correction, Kidder (1976) found the need for additional adjustments. To solve these problems, Kidder determined the mean brightness temperature for the 3 months (December 1972–February 1973) at each scan angle for 10° × 10° grid box over the Pacific Ocean. Then the difference between the mean brightness temperature at scan angle θ and the mean brightness temperature at nadir was averaged over all grid boxes. These scan-angle correction temperatures were subtracted from the original brightness temperature. Another scan-angle correction by Rao (1984) simply assumed that satellite brightness temperatures decreased by 2.1 K from nadir to 30°, linearly with scan angles. Scan angles greater than 30° were ignored in the retrieval. Short (1988) applied an empirical correction for the scan-angle bias of the form

$$\bar{T}(\theta, \text{new}) = \bar{T}(\theta, \text{old}) - 45(\sec\theta - 1), \quad (1)$$

where $\bar{T}$ is the field-of-view (FOV) averaged brightness temperature, and θ is the scan angle. Shin et al. (1990) used only 21 pixels near nadir (scan positions 29–49 corresponding to ±12° scan angles), which have very little bias; hence, no scan-angle correction was deemed necessary in their analysis. The resulting reduced swath width, of course, increased sampling errors.

In this study, we have attempted to achieve monthly 5° × 5° area-averaged rain rate over the tropical oceans from January 1973 to December 1976 using the ESMR-5 data. The approach is an extension of the work of Shin et al. (1990) by including all angles of the cross-track scanner in order to reduce sampling error. Consequently, we have developed a method to remove the scan-angle bias from the retrieved rainfall product.

The ESMR-5 data include the El Niño events of 1972–73 and 1976–77. Many investigators (Rasmusson and Carpenter 1982; Rasmusson and Wallace 1983; Ropelewski and Halpert 1987) reported that precipitation patterns are drastically changed during El Niño/Southern Oscillation (ENSO). We also have explored some change of the distribution of rainfall during ENSO during retrieved rain rate.

As discussed above, there are clearly difficulties with the ESMR-5 data that have been resolved with subsequent instruments. As a result, many ad hoc assumptions are necessary to retrieve rainfall from the ESMR-5 data. However, during the time period of this study, ESMR-5 was the only appropriate imaging microwave radiometer in earth orbit; we believe the atmospheric events of the time period in question justify the effort.

2. Data

The data used for this study are obtained from ESMR-5 measurements. The ESMR-5 was on board Nimbus, which was launched 11 December 1972. The

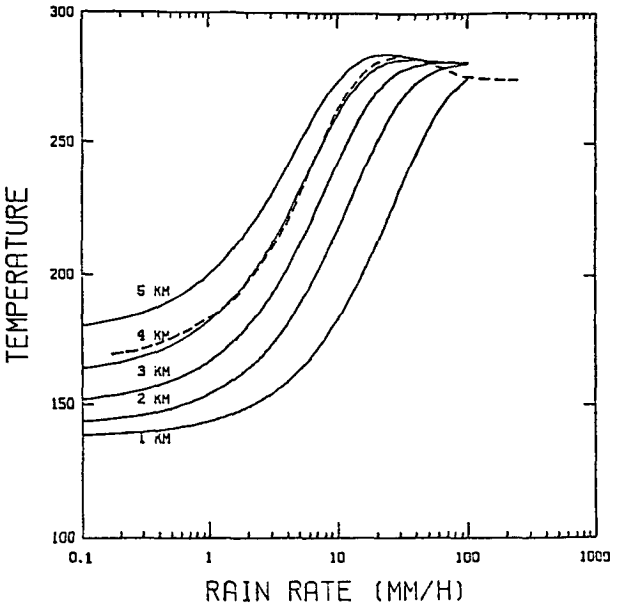

FIG. 1. The 19.35-GHz brightness temperature versus rain rate for various freezing levels. The broken line is that of the Wilheit curve without scattering (from Shin et al. 1990).

instrument performed satisfactorily most of the time from January 1973 to December 1976. It was the first microwave imager to be flown in space. The ESMR-5 measured the radiance of horizontally polarized radiation within a narrow band centered at 19.35 GHz (1.55 cm). Its antenna scanned electrically across the subpoint track of the satellite, from 50° to the left of nadir, through nadir, to 50° to the right in 78 steps, every 4 s. The horizontal resolution varied in size from 25 km × 25 km near nadir to 45 km × 160 km at the left and right extremes of the scan. It flew in a near-polar sun-synchronous circular orbit at an altitude of approximately 1100 km with near local noon (ascending) and midnight (descending) equator crossing times. More detailed information about ESMR-5 instrument is compiled in Wilheit (1972).

The brightness temperature is the temperature that a blackbody would have to have in order to emit the same amount of radiant energy detected by the sensor. For the ESMR-5 instrument the measured radiant energy is within a narrow band centered at 19.35 GHz. The brightness temperature depends upon the emission from the earth's surface, which is changed by the intervening atmosphere between the earth and the satellite. The emissivity is a function of dielectric constant of the emitting surface, surface roughness, and the radiometer viewing angle. In the 19.35-GHz region, the emissivity of land surface is large ($\sim$0.9) and variable, but that of ocean (ϵ_w) is small ($\sim$0.4) and more or less uniform. In the vicinity of 19.35 GHz, $\epsilon_w \propto T_w^{-1}$, where T_w is the thermodynamic temperature of the water surface, with the result that the brightness temperature ($\epsilon_w T_w$) of a smooth water surface is virtually independent of the thermodynamic temperature of the surface layer of the water. Thus, the ocean is a good background for observing the intervening atmosphere. Areas of precipitation can be detected by the ESMR-5 over an uniform ocean background (Theon 1973; Wilheit

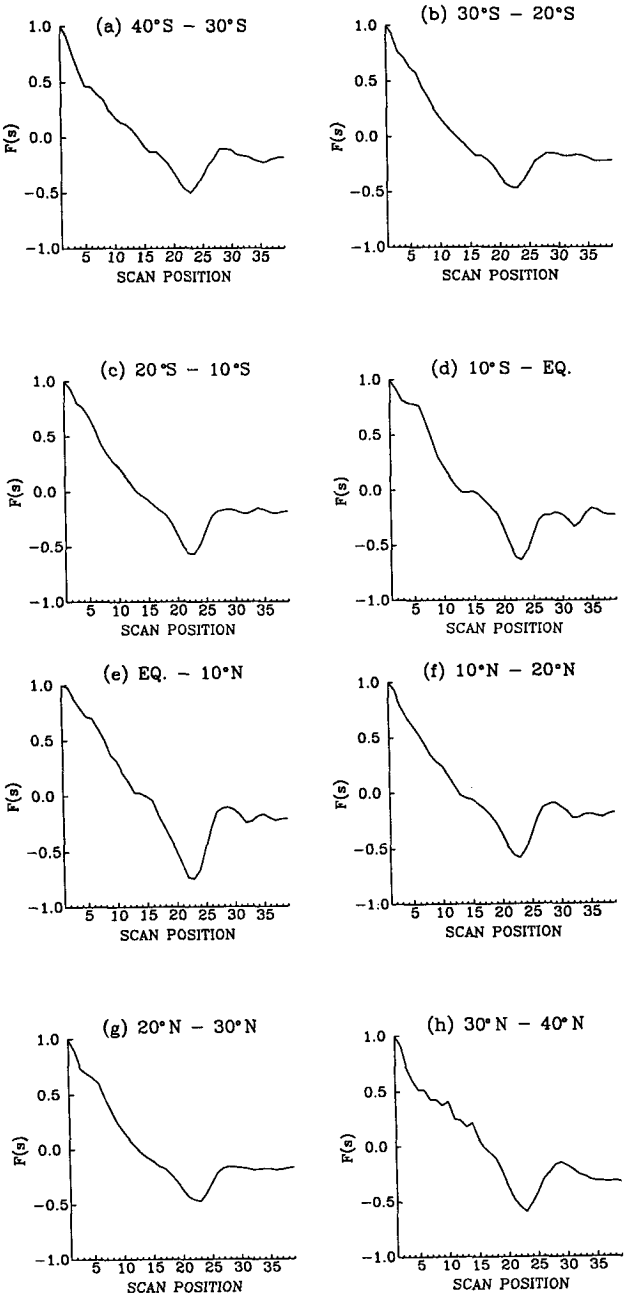

FIG. 2. Normalized zonal mean of deviations from 39 scan average versus scan position. (a) Latitude band 40°–30°S, (b) 30°–20°S, (c) 20°–10°S, (d) 10°S–0°, (e) 0°–10°N, (f) 10°–20°N, (g) 20°–30°N, and (h) 30°–40°N.

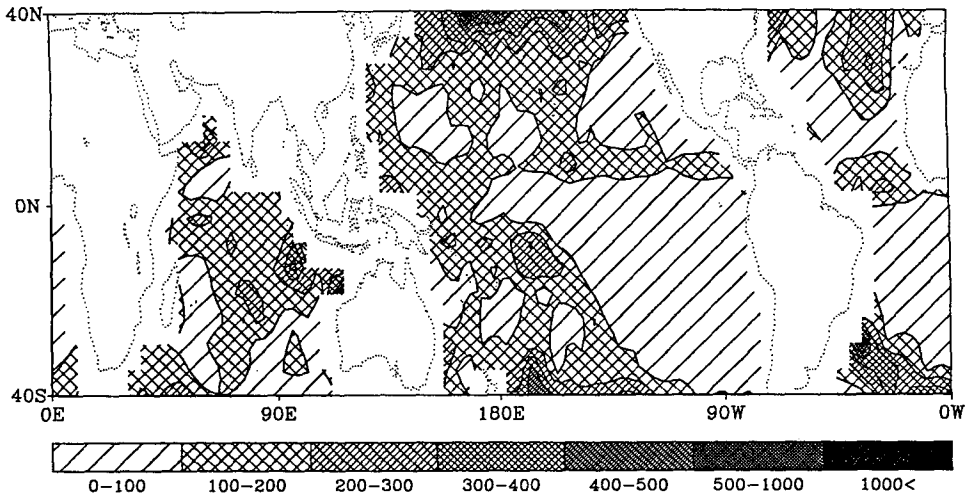

FIG. 3. The unbiased monthly rainfall (mm month^{-1}) for December 1973. Contour interval is 20 mm month^{-1}. Bold lines are drawn for every 100 mm month^{-1}. Shading denotes rainfall less than 100 mm month^{-1}.

et al. 1973), but over land, the detection of rain is more difficult (Sabatini and Merritt 1973).

The ESMR-5 had calibration problems associated with scan angles and solar heating and cooling cycle. The scan-angle bias caused by the cross polarization grating lobe was mentioned in section 1. A bending in the antenna deployment mechanism due to differential solar heating and cooling cycles introduced 100-km location errors (Allison et al. 1974). In scan positions 36–43, the average difference due to instrumental problems between the noon and midnight brightness temperature was found to be about 4 K. Thus, Shin et al. (1990) applied an additional correction to those scans by adding 4 K to midnight observations. Kidder (1976) and Short (1988) also applied a similar correction factor. The ESMR-5 dataset was reprocessed by Lee and Byerly (1981) to correct location errors and to identify instrument malfunctions. They developed algorithms to identify earth location errors and to apply corrections based on simulated orbits superimposed on equator crossing locations. The averaging of selected orbits in 1973 and 1974 was used to generate this model because equator crossing data in later years were not available. Nevertheless, Short and North (1990) found that the reprocessed data still have some location errors (about 40 km) and a scan-angle bias.

3. Retrieval of monthly rainfall and scan-angle adjustment

a. Retrieval of precipitation

On the assumption that scan-dependent errors are symmetric relative to the nadir, the ESMR-5 brightness temperatures for paired scans (e.g., scan 1 and scan 78, scan 2 and scan 77, . . . , scan 39 and scan 40) were collected for each month (from January 1973 to December 1976) and every 5° × 5° grid box over the global oceans 40°S–40°N. The data for 5° × 5° grid boxes having land, major islands, and coastlines were eliminated in processing. Then the collected brightness temperatures for each paired scan position, each grid box, and each month were collected into histograms with 2-K bins. As in Shin et al. (1990) it is assumed that the histograms are composed of the sum of a normal distribution of nonraining (background temperature) pixels and a gamma distribution of brightness temperature in raining pixels. Using the peak as a first guess of the mean of the normal distribution, the variances of background temperatures are calculated. An iterative method was used to search for a best fit to the histogram. The rain distribution was recovered when the normal distribution was subtracted from the histogram.

Shin et al. (1990) modified the radiative transfer model of Wilheit et al. (1977) by calculating the emissivity of the ocean surface following the facet model of Wilheit (1979). This calculation used the distribution of sea surface slopes as a function of wind speed determined by Cox and Munk (1955) and modified by Hollinger (1971) for microwave frequencies. In addition, the model of Shin et al. (1990) has no scattering. Figure 1 shows the calculated brightness temperature at 19.35 GHz versus rain rate from this model for freezing levels of 1–5 km. The rain rate and brightness temperature (R–T) relationship from this model can be summarized by

$$T_B(R) = 281 - Be^{-C(z)R}, \qquad (2)$$

TABLE 1. Statistics for the ESMR-5 rain estimates as compared to rain gauge rain estimates over the tropical Pacific.

	Station	Latitude	Longitude	Correlation	95% significance
Equatorial W. Pacific	Koror	7.33°N	134.48°E	0.46	n
	Yap	9.48°N	138.08°E	0.27	n
	Truk	7.47°N	151.85°E	0.16	n
	Kwajal	8.73°N	167.73°E	0.12	n
Equatorial dry zone	Banaba	0.90°S	169.55°E	0.41	n
	Majuro	7.08°N	171.38°E	0.47	n
	Butari	3.12°N	172.80°E	0.39	n
	Tarawa	1.35°N	172.93°E	0.54	y
	Nanumea	5.67°S	176.11°E	0.68	y
	Nui	7.25°S	177.15°E	0.85	y
	Nukufet	8.03°S	178.03°E	0.77	y
	Funafu	8.52°S	179.20°E	0.85	y
	Nukuno	9.20°S	171.92°W	0.74	y
	Fanning	3.85°N	159.37°W	0.79	y
	Penrhyn	9.00°S	158.05°W	0.77	y
	Christm	1.98°N	157.48°W	0.77	y
SPCZ	Niulak	10.78°S	179.47°E	0.64	y
	Haapai	19.80°S	174.35°W	0.48	n
	Keppel	15.95°S	173.77°W	0.40	n
	PukaII	10.88°S	165.82°W	0.88	y
	Palmerst	18.07°S	163.17°W	0.61	y
	Rakahang	10.05°S	161.10°W	0.61	y
	Atiutaki	18.82°S	159.77°W	0.44	n
	Rangiroa	14.97°S	147.67°W	0.51	y
	Takaroa	14.48°S	145.03°W	0.59	y
	Hao	18.06°S	140.97°W	0.49	y
	Pukapuka	14.80°S	138.82°W	0.55	y
Extratropics	Wake	19.28°N	166.65°E	0.14	n
	Johnston	16.73°N	169.50°W	0.61	y
	Aroa	21.25°S	159.82°W	0.34	n
	Mauke	20.13°S	157.35°W	0.36	n
	Herehere	19.87°S	145.00°W	0.21	n
	Moruroa	21.82°S	138.80°W	0.56	y
	Tureia	20.77°S	138.55°W	0.29	n

where $C = 0.004 + 0.026z + 0.0045z^2$, z is the freezing-level height (km), and B is the dynamic range of given background temperature. Similar to Rao et al. (1976), we found some difficulty with this model when using the zonally symmetric climatological freezing-level heights from Oort and Rasmusson (1971) and Taljaard et al. (1969). To avoid this problem Rao et al. (1976) used an ad hoc correction. Wilheit et al. (1991) determined monthly mean freezing-level heights from the 19.35- and 22.235-GHz brightness temperature histograms for raining conditions. Although it is for a different year, this estimated freezing level is used in this study.

For this study the rain rate is estimated ($\hat{R}$) at each 5° × 5° grid box by

$$\hat{R} = P \sum_{i}^{N} f(T_i)\hat{R}_i(T_i), \qquad (3)$$

where P (rain probability) is the ratio of the number of rain pixels to the total in the histogram, $f(T_i)$ is the probability density function of brightness temperatures when raining, and $\hat{R}_i(T_i)$ is the estimated rain rate at the ith brightness temperature of the bin. The systematic underestimate of rain rate, called the beam-filling error, is due to the inhomogeneity of rain rate over the FOV combined with the nonlinear R–T relationship. Smith and Kidder (1978), Lovejoy and Austin (1980), Rosenkranz (1982), and Gloersen et al. (1984) reported this problem in their studies. Short (1988) (also Short and North 1990; Chiu et al. 1990) suggested a beam-filling correction factor for the ESMR-5 data may vary from 1.5 to 2.8 as the rain-rate regime varies from suppressed to active convective. As in Shin et al. (1990), a factor of 2.2 is applied to the estimated rain rate.

b. *Scan-angle adjustment*

Because of missing months in the data, only 28 months of monthly rainfall are retrieved. The following functional form is calculated in each 5° × 5° grid box:

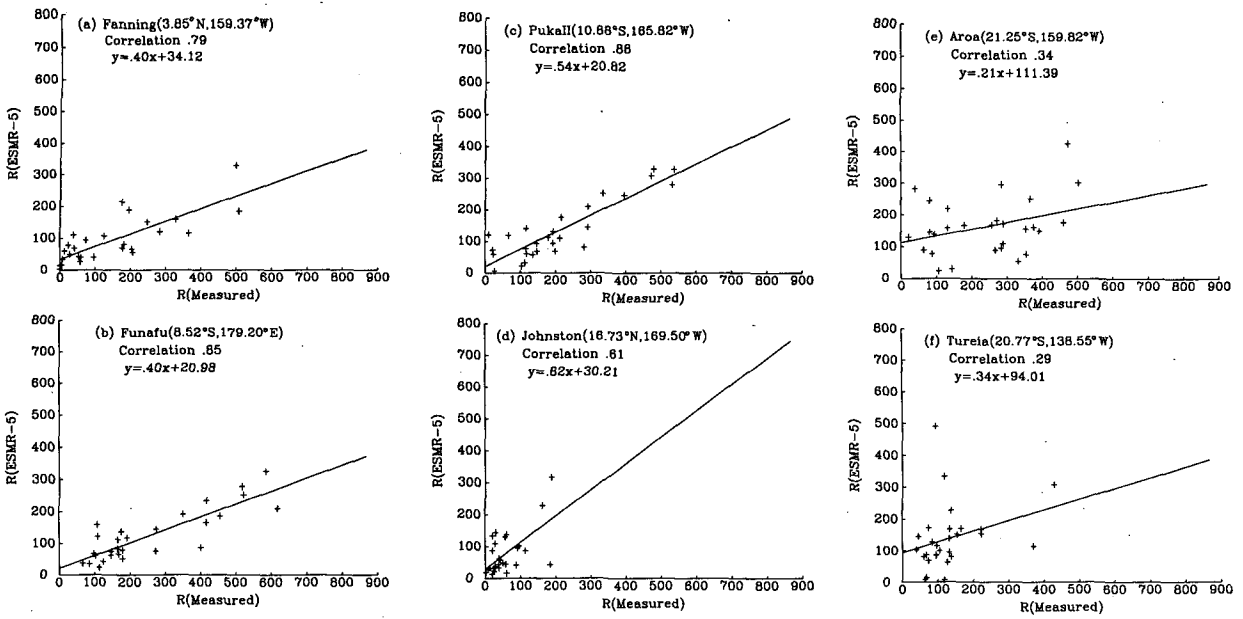

FIG. 4. Scatterplots of the island station rainfall versus ESMR-5-inferred rainfall at (a) Fanning (3.85°N,159.37°W), (b) Funafu (8.52°S,179.20°E), (c) PukaII (10.88°S,165.82°W), (d) Johnston (16.73°N,169.50°W), (e) Aroa (21.25°S,159.82°W), and (f) Tureia (20.77°S,138.55°W).

$$f(s) = \hat{R}(s) - \frac{1}{39}\sum_{i=1}^{39} \hat{R}(i)$$

$$s = 1, 2, 3, \cdots, 39, \quad (4)$$

where $\hat{R}(s)$ is the estimated rain rate at each scan position. Thus, this value represents the deviation at each scan position from mean through all scans. The maximum value was normalized to unity after the 28-month means for each 10° latitude band were calculated. It will be referred to here as a scan correction phase function. These results are shown in Fig. 2. They are very similar once the normalization is included.

We adopt the model

$$\hat{R}(s) = A(\text{lat, long})F(s) + \bar{R}$$

$$s = 1, 2, 3, \cdots, 39, \quad (5)$$

where $\bar{R} = (39)^{-1}\sum_{i=1}^{39} \hat{R}(i)$, $F(s)$ is a universal scan correction phase function and A(lat, long) is a constant independent of scan angle that is derived on the basis of the available 28 months of data. This allows a universal $F(s)$ to be calculated for the entire dataset. On the assumption that the estimated rain rate at nadir is correct, the rainfall bias $B(s)$ for scan angle as compared to nadir can be calculated:

$$\begin{aligned} B(s) &= \hat{R}(s) - \hat{R}(39) = A(\text{lat, long})F(s) \\ &\quad + \bar{R} - [A(\text{lat, long})F(39) + \bar{R}] \\ &= A(\text{lat, long})[F(s) - F(39)] \end{aligned}$$

$$s = 1, 2, 3, \cdots, 39, \quad (6)$$

where $\hat{R}(39)$ is the rainfall at nadir, and $F(39)$ is the phase function at nadir. We may obtain the corrected rainfall $\hat{R}_c$ for each 5° × 5° by combining (5) and (6). This leads to

$$\begin{aligned} \hat{R}_c &= \hat{R}(s) - B(s) = A(\text{lat, long})F(s) \\ &\quad + \bar{R} - A(\text{lat, long})[F(s) - F(39)] \\ &= \bar{R} + A(\text{lat, long})F(39) \end{aligned}$$

$$s = 1, 2, 3, \cdots, 39, \quad (7)$$

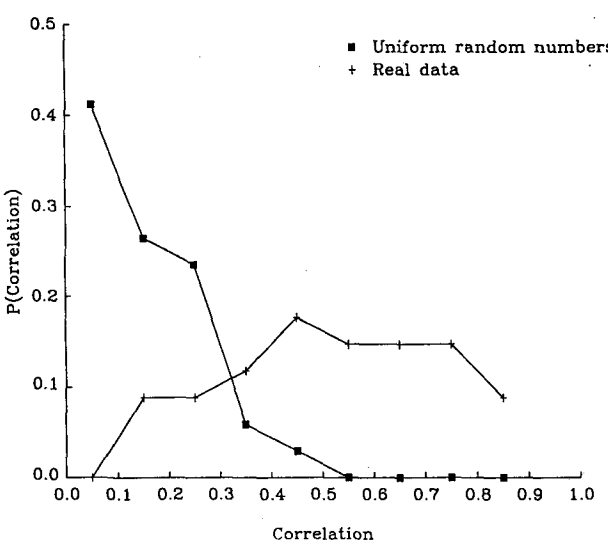

FIG. 5. Probability polygons of correlation coefficients for uniform random numbers and real data.

when $\hat{R}_c$ was calculated, and the 28-month global mean $F(39)$ was used. This is due to the globally similar pattern of the phase function. We can now sum up (5) to find $A(\text{lat, long})$:

$$\sum_{s=1}^{39} [\hat{R}(s) - \bar{R}]^2 = \sum_{s=1}^{39} [A(\text{lat, long})]^2[F(s)]^2$$

$$= [A(\text{lat, long})]^2 \sum_{s=1}^{39} [F(s)]^2$$

$$= [A(\text{lat, long})]^2 F_0, \qquad (8)$$

where $F_0 = \sum_{s=1}^{39} [F(s)]^2$. Therefore, by (8), $A(\text{lat, long})$ is given by

$$A(\text{lat, long}) = \left\{ \frac{\text{var}[\hat{R}(s)]}{F_0} \right\}^{1/2}, \qquad (9)$$

where $\text{var}[\hat{R}(s)] = E\{[\hat{R}(s) - \bar{R}]^2\}$. To find F_0, $E\{[F_{\text{lat}}(s) - F_{\text{gm}}(s)]^2\} = \text{var}[F_{\text{lat}}(s)]$ is calculated, where $F_{\text{lat}}(s)$ is the phase function at some latitude band and $F_{\text{gm}}(s)$ is global mean phase function. To find the best-fitting scan correction phase function, the smallest $\text{var}[F_{\text{lat}}(s)]$ latitude band (10°–20°N) is taken along with F_0 into (9) and we obtain $A(\text{lat, long})$. The obtained $A(\text{lat, long})$ can be substituted into (7) to calculate the rain rate with scan-angle bias removed.

Figure 3 shows the unbiased rainfall for December 1973. These values have been multiplied by the beam-filling correction factor of 2.2. The South Pacific convergence zone (SPCZ) and the narrow band of the intertropical convergence zone (ITCZ) are clearly visible. Rainfall is overestimated at higher latitudes because of the globally uniform beam-filling correction factor we used. Because the statistics of extratropical rainfall (stratiform rain) are different from those of tropical rainfall (convective rain), we probably should use a different beam-filling correction factor. However, we have no data on which to base a regionally and seasonally varying beam-filling correction.

TABLE 2. Statistics for the monthly rainfall from island stations.

Reference station	Mean	Standard deviation	Station	Correlation
Christmas	165.4	158.8	Tarawa	0.59
			Koror	−0.43
			Haapai	−0.01
Tarawa	78.9	115.2	Christmas	0.59
			Koror	−0.27
			Haapai	−0.08
Koror	312.3	136.7	Christmas	−0.43
			Tarawa	−0.27
			Haapai	−0.09
Haapai	162.8	119.5	Christmas	−0.01
			Tarawa	−0.08
			Koror	−0.09

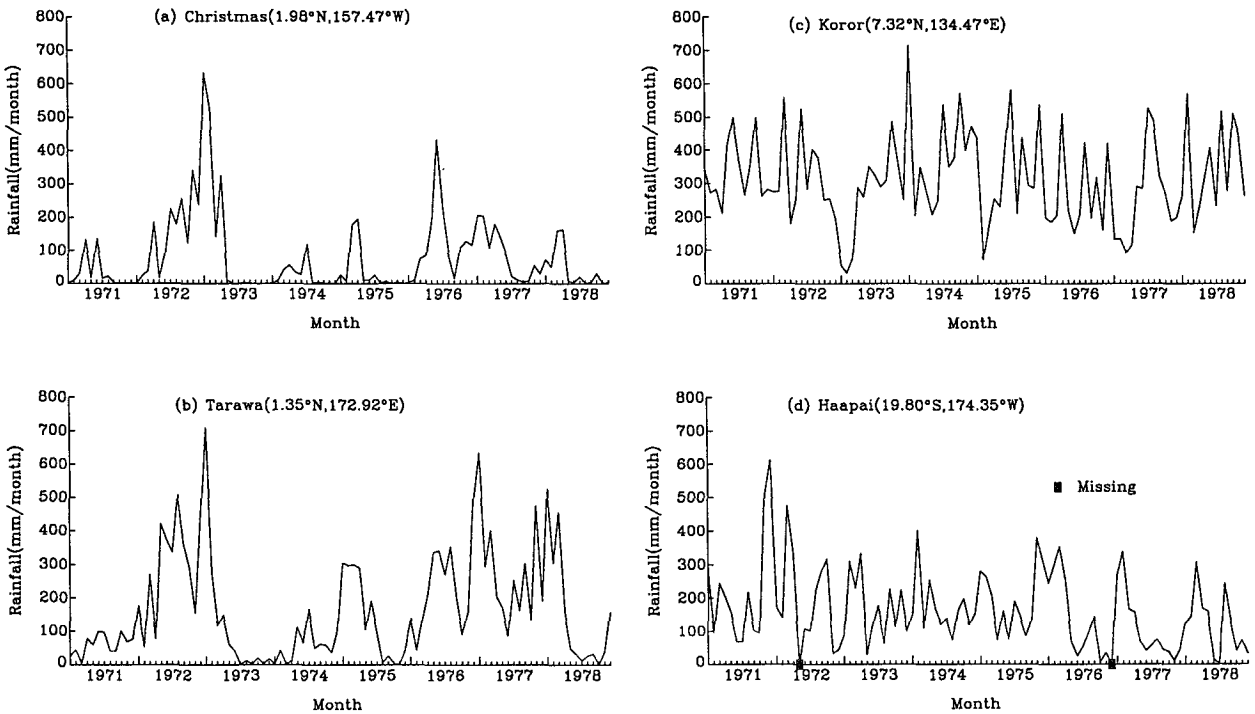

FIG. 6. Time series of rainfall (mm month^{-1}) at (a) Christmas (1.98°N,157.47°W), (b) Tarawa (1.35°N,172.92°E), (c) Koror (7.32°N,134.47°E), and (d) Haapai (19.80°S,174.35°W). The large tick marks denote January.

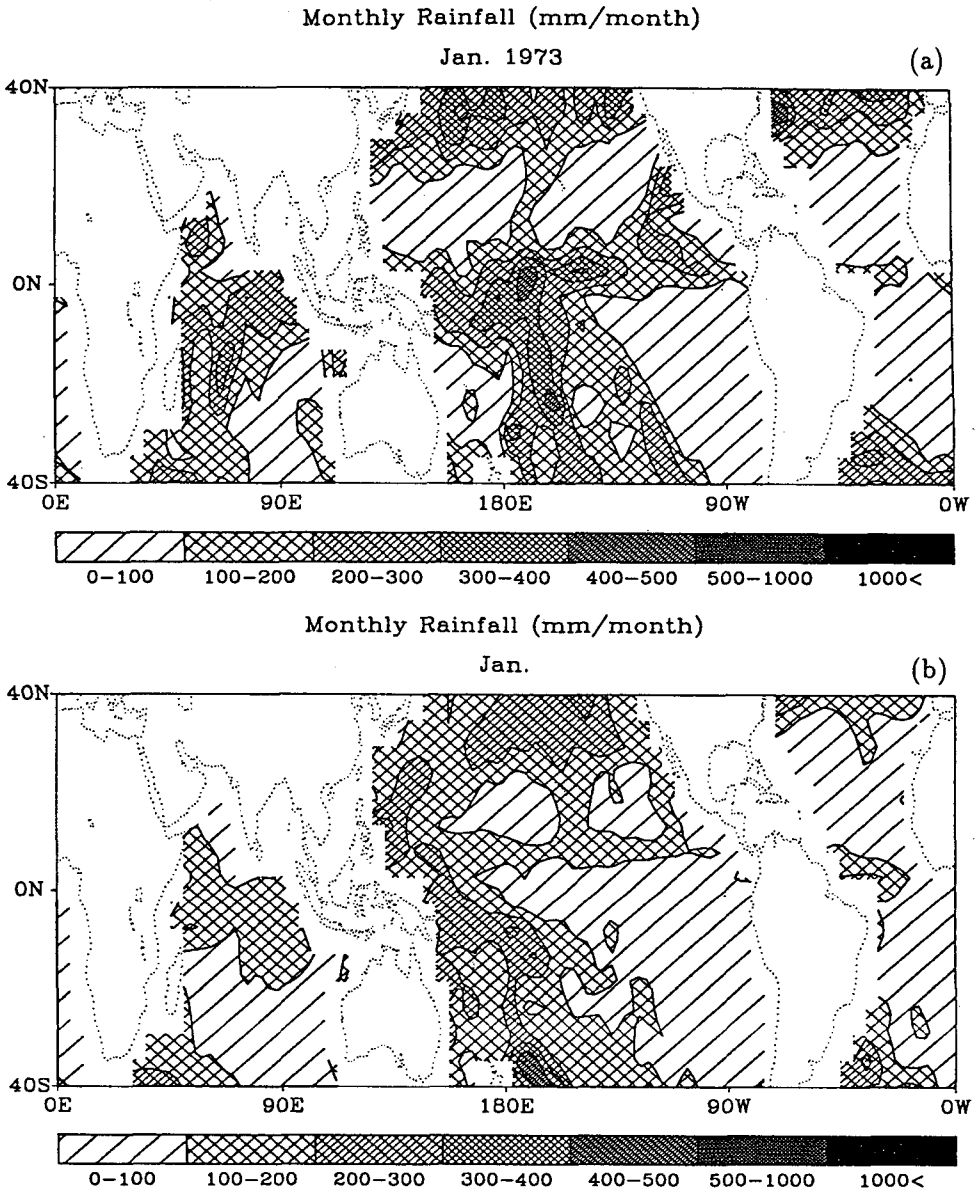

FIG. 7. The rainfall (mm month^{-1}) for (a) January 1973 and (b) mean of January during non-El Niño years. (c) Rainfall anomaly for January 1973, values in (a) minus (b). Contours are drawn every 50 mm month^{-1} with a bold zero line. Dashed lines denote negative anomalies.

4. Verification of retrieved rain rate

Island station rainfall measurements over the Pacific were used to verify the retrieved monthly rainfall. Morrissey and Greene (1991) collected the data from several sources on tape and manuscript format. Only data complete for the month were included. Otherwise, it was listed as missing (−999). The data available at Oklahoma Climate Survey began in January 1971 and ended in December 1990. The atoll stations are scattered throughout the Pacific.

Island stations are classified into four groups based on geographical location and similar rainfall climate. The correlation coefficients between rain gauge data and ESMR-5 inferred rainfall are shown in Table 1. When the correlation coefficients are calculated, the 5° × 5° grid boxes cover each one of these islands. The correlation coefficients were tested at the 95% significance level. Although this is not an exact comparison, the correlation is remarkably high in the equatorial dry zone and SPCZ. In the extratropics and equatorial western Pacific, the correlation is low.

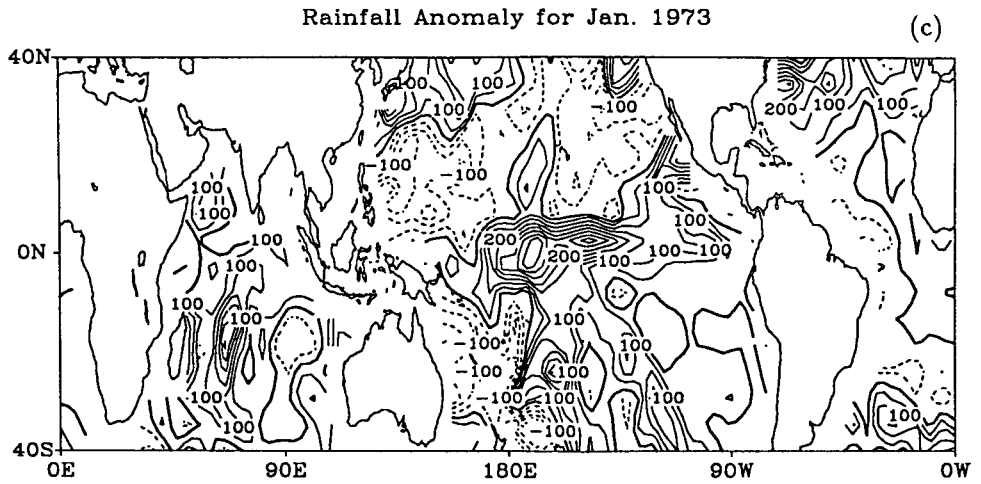

FIG. 7. (*Continued*)

Monthly rainfall data from island stations and ESMR-5 are also compared in the form of scatter diagrams in Fig. 4. Six island stations were selected for the following reasons. These islands are situated in well-defined climatological regimes ranging from the equatorial dry zone (Fanning, Funafu), SPCZ (PukaII), and extratropics (Johnston, Aroa, Tureia). Slopes should be 1 but are not. These discrepancies are resulted from sampling error due to temporal gaps in the satellite observations. Another point to be considered is that an island rain gauge measurements cannot represent average rainfall for each 5° × 5° grid box. One is a point measurement; the other is an area average.

To demonstrate the statistical significance of the results, 28 pairs of uniform random numbers were generated and sample correlation coefficients were calculated. This procedure was repeated for a sample size equal to the total number of stations. The probability polygons (normalized histograms) are constructed for the correlation coefficient (Fig. 5). The correlation coefficients of uniformly distributed random numbers have a reverse *J*-shaped distribution with a maximum occurring at one end (correlation of 0.05) and most values are distributed below 0.35. However, the correlation coefficients between rain gauge data and ESMR-5-inferred rainfall have a bell-shaped distribution that has a maximum at 0.45. The dissimilarity of these two distributions is taken as strong evidence that the satellite retrievals of rain rate are statistically significant.

5. Change of precipitation patterns associated with the 1972–73 and 1976–77 El Niño events

Because the ESMR-5 data include only 4 years (January 1973–December 1976), 8 years (January 1971–December 1978) of monthly rainfall data from the island stations are used to demonstrate the trend of rainfall associated with El Niño (Fig. 6). These islands are situated in well-defined climatological regimes ranging from the central equatorial Pacific (Christmas), near the equatorial dateline (Tarawa), western equatorial Pacific (Koror), and SPCZ (Haapai). There is a remarkably positive rainfall change at Christmas and Tarawa Islands in the intense 1972–73 El Niño (March 1972–March 1973). There is also a large positive rainfall change in the moderate 1976–77 El Niño (February 1976–January 1977). At Koror Island, where heavy precipitation is observed normally, there is a remarkably negative rainfall change between January and March 1973. From January 1977 to April 1977 rainfall shows a decrease. At Haapai Island, there is a little decrease of rainfall. Table 2 shows the average, standard deviation, and one-point correlation coefficients. The Christmas and Tarawa Islands, which are located in the equatorial dry zone, have high standard deviation. As expected, rainfall in the central equatorial Pacific and western equatorial Pacific shows a relatively high negative correlation coefficient.

Monthly mean maps of precipitation over the oceans have been estimated from ESMR-5 data obtained during the non–El Niño years April 1973 to December 1975. These maps depict normal conditions during quiet time. It is recognized that the normal conditions do not truly represent a long-term climatology, but contain additional anomalies themselves. In order to illustrate the spatial variations produced by the El Niño, deviations with respect to these mean maps are derived. Figures 7a, 7b, and 7c show the distribution of rainfall for January 1973, mean of January during non–El Niño years, and the deviations in rainfall for January 1973. The expected features such as the increase of rainfall over the eastern and central equatorial Pacific Ocean and decrease of precipitation over the equatorial western Pacific Ocean and eastern Australia are visible.

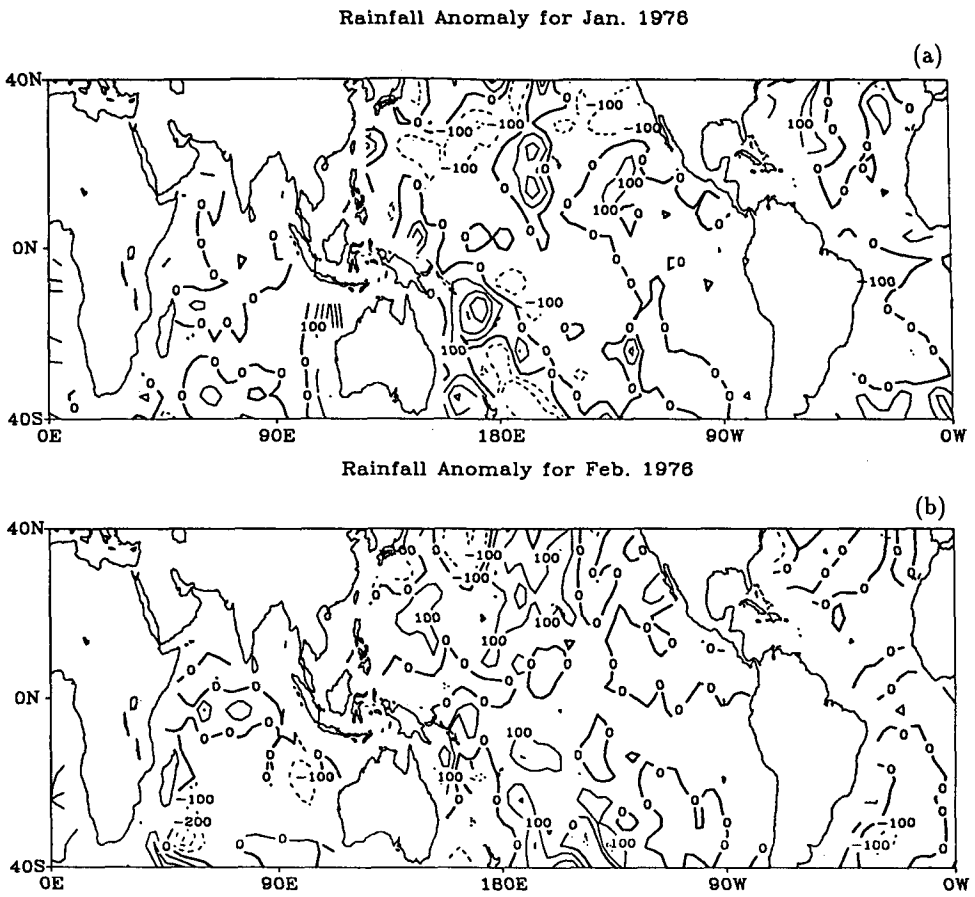

FIG. 8. The rainfall anomaly for (a) January 1976, (b) February 1976, (c) April 1976, (d) August 1976, (e) September 1976, and (f) October 1976. Contours are drawn every 100 mm month^{-1} with a bold zero line. Dashed lines denote negative anomalies.

Prabhakara et al. (1986) found comparable negative (over the equatorial western Pacific) and positive (over the equatorial eastern and central Pacific) anomalies from SMMR-inferred changes of rainfall patterns during the 1982–83 El Niño. However, the OLR negative anomaly is about one-half of the positive anomaly during the 1982–83 El Niño (Rasmusson and Wallace 1983). The El Niño 1972–73 was at its peak in December 1972 and January 1973 and lasts until March 1973. Unfortunately, only January 1973 is available for study of the 1972–73 El Niño event.

The sequence of anomaly maps for 1976 is shown in Fig. 8. Because of missing months, the sequence is discontinuous. The deviation is calculated as relative to the non–El Niño years April 1973 to December 1975. Over the central and eastern equatorial Pacific Ocean, the positive anomalies started to appear in April and extended during August and September. These results are very consistent with enhanced convection that was observed by Liebmann and Hartmann (1982). The negative anomalies over the western Pacific and eastern Australia appear in April, disappear until September, and then reappear in October.

Monthly mean zonal averages on the eastern Pacific from the date line to the coast of North and South America are plotted from January 1973 to October 1976 (Fig. 9) to highlight the ESMR-5-inferred rainfall anomalies. The anomalies derived during the non–El Niño years April 1973 to December 1975 are all zero; therefore, those periods are excluded. Well-defined positive anomalies are visible near the equator in January 1973 and from August 1976 to October 1976. Wyrtki (1979) found that the 1972–73 El Niño was much stronger and that the 1976–77 event occurred largely in the Northern Hemisphere. From this figure we cannot be definitive because of insufficient data. However, this result is very consistent with previous works (Quinn et al. 1978; Wyrtki 1979).

6. Conclusions

This study has proposed an algorithm to estimate monthly 5° × 5° area-averaged rain rate over the

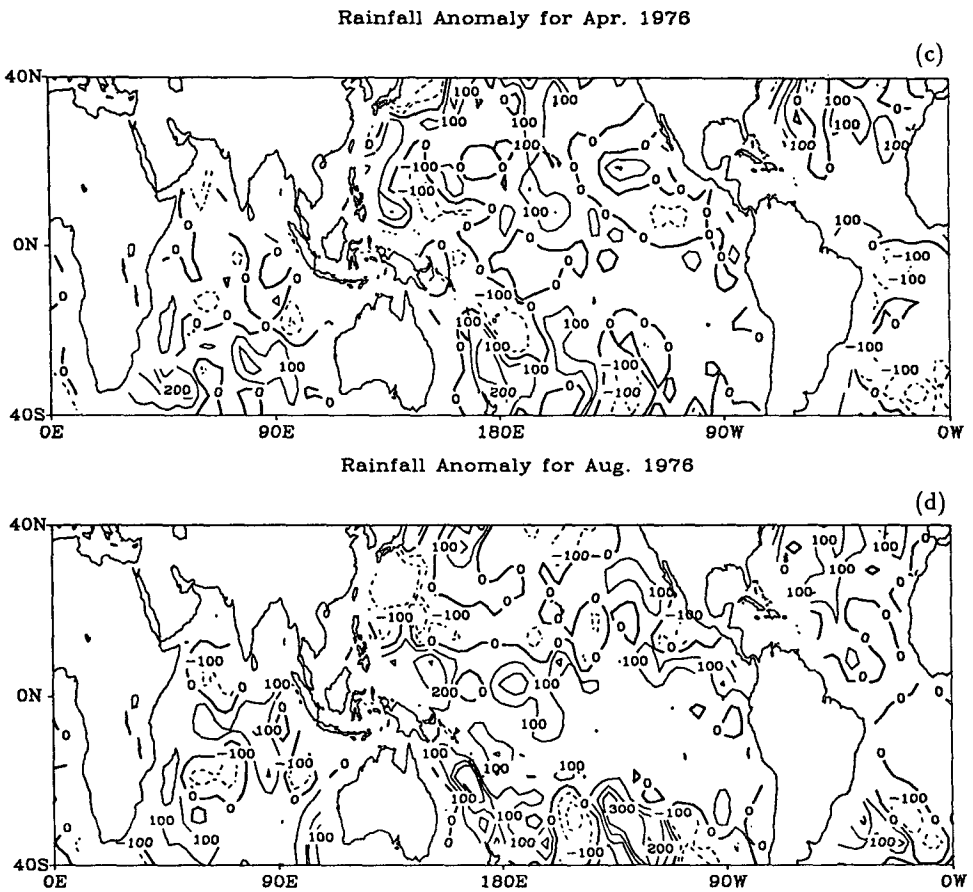

FIG. 8. (*Continued*)

oceans using single-channel microwave data from the *Nimbus-5* satellite. Unlike previous works, the ESMR-5 data with all scan angles (from −50° to 50°) were used in this study. The estimated rain rates have a scan-angle dependence due to variable antenna sidelobe effects, surface emissivity, and propagation pathlength. This scan-angle bias was eliminated using a statistical method. In addition, the nonlinear rain rate and brightness temperature relationship and inhomogeneity of the rain rate within the FOV result in an underestimation of the rain rate called the beam-filling error. Because a globally uniform beam-filling correction factor of 2.2 is multiplied, an overestimation of rainfall is found in high latitudes, due to different characteristics of rain such as convective rain in the Tropics and stratiform rain in the extratropics.

The retrieved monthly rainfall was verified using island station rainfall measurements over the Pacific. The correlation coefficients between the two datasets are remarkably high in the equatorial dry zone and SPCZ but low in the extratropics. In the scatterplots of the island station rainfall versus ESMR-5-inferred rainfall, slopes should be 1 but are not. Because rainfall is highly variable in space and time, comparisons between instantaneous rain rate at one point and time- and area-averaging rain rate result in errors. Therefore, it is very important to develop a validation scheme using "ground truth" data. Judging from different slopes in the different region, in the Tropical Rainfall Measuring Mission, ground-truth sites should be located at several representative points.

The ESMR-5-inferred rain-rate data include the strong 1972–73 El Niño and moderate 1976–77 El Niño. Generally, during El Niño events precipitation patterns as well as wind field and sea surface temperature are dramatically modified. The rainfall deviations with respect to monthly mean of precipitation during the non–El Niño years April 1973 to December 1975 showed an increase of rainfall over the eastern and central equatorial Pacific Ocean and decrease of precipitation over the equatorial western Pacific Ocean and eastern Australia. The rainfall anomaly of the 1972–73 El Niño is much stronger than that of 1976–77 El Niño. Thus, the ESMR-5-inferred rainfall data over the ocean are useful for

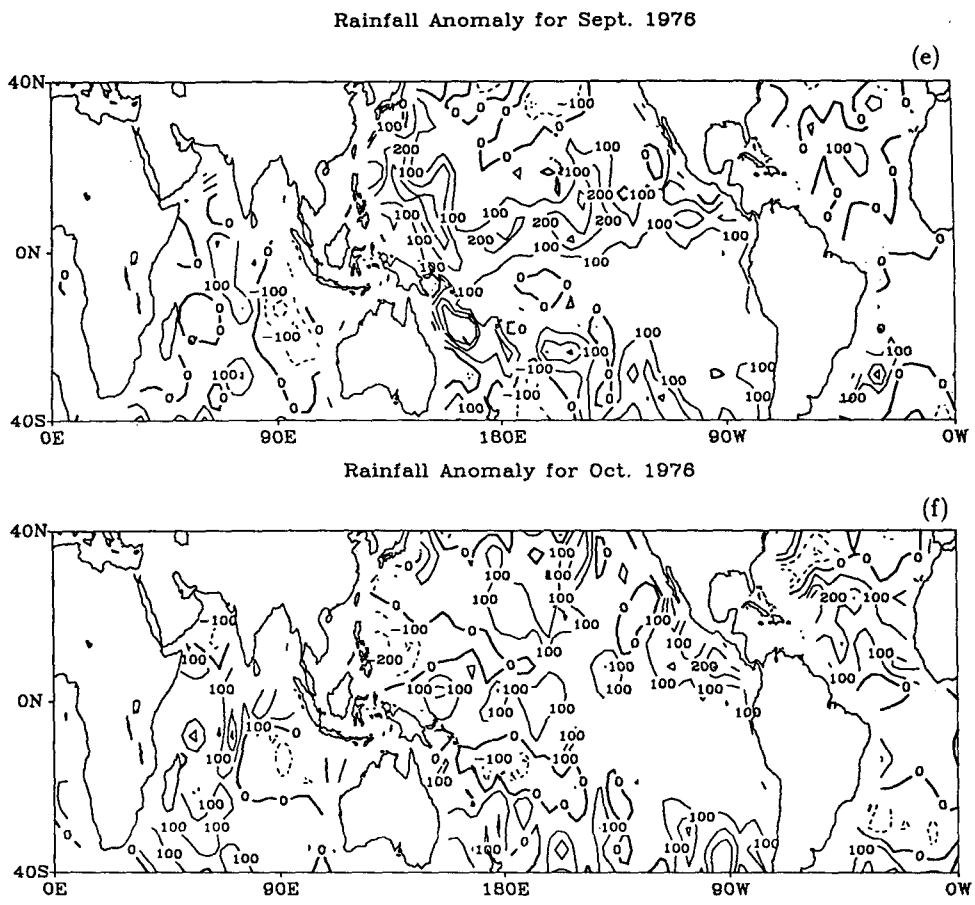

FIG. 8. (*Continued*)

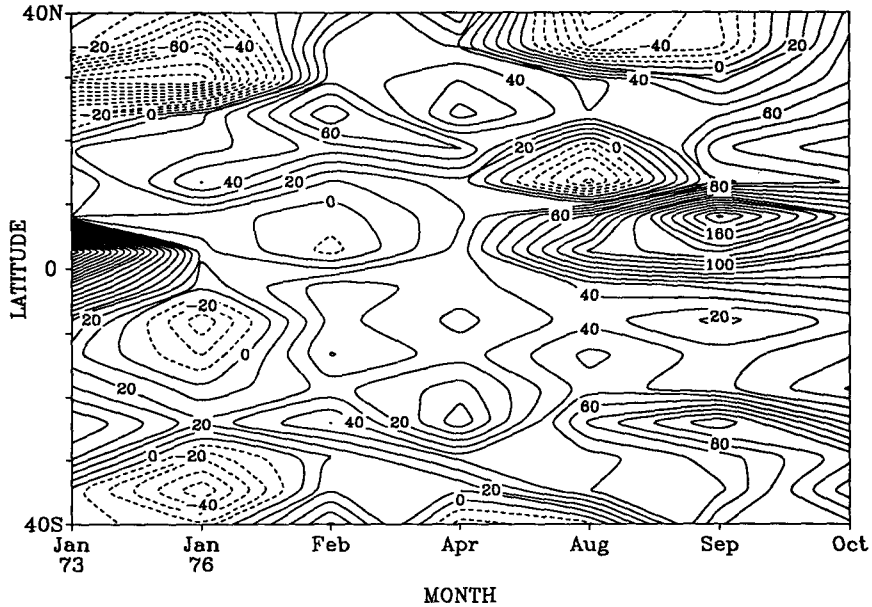

FIG. 9. Latitude–time plot of zonal mean of ESMR-5-inferred rainfall anomalies (mm month^{-1}) between the date line and the coast of North and South America during El Niño years. Contours are drawn every 10 mm month^{-1}. Dashed lines denote negative anomalies.

global precipitation climatology and for the studies of the El Niño events.

Acknowledgments. We would like to thank Dr. Mark L. Morrissey for providing the island station rainfall data. We also gratefully acknowledge the support from NASA via the TRMM science team.

REFERENCES

Allison, L. J., E. B. Rodgers, T. T. Wilheit, and R. Wexler, 1974: A multi-sensor analysis of Nimbus 5 data on 22 January 1973. NASA X-910-74-20, Goddard Space Flight Center, Greenbelt, MD. [NTIS N74-22115/1.]

Chiu, L. S., G. R. North, D. A. Short, and A. McConnell, 1990: Rain estimation from satellites: Effect of finite field of view. *J. Geophys. Res.*, **95,** 2177–2185.

Cox, C., and W. Monk, 1955: Some problems in optical oceanography. *J. Mar. Res.*, **4,** 63–78.

Gloersen, P., D. J. Cavalieri, A. T. C. Chang, T. T. Wilheit, W. J. Campbell, O.-M. Johannessen, K. B. Katsaros, K. F. Kunzi, D. B. Ross, D. Staelin, E. P. L. Windsor, F. T. Barath, P. Gudmandsen, E. Langham, and R. O. Ramseier, 1984: A summary of results from the first Nimbus 7 SMMR observations. *J. Geophys. Res.*, **89,** 5335–5344.

Hollinger, J. P., 1971: Passive microwave measurements of sea surface roughness. *IEEE Trans. Geosci. Electron.*, **9,** 165–169.

Kidder, S. Q., 1976: Tropical oceanic precipitation frequency from Nimbus 5 microwave data. Atmospheric Science Paper 248, Colorado State University, Fort Collins, CO. [NTIS N76-26763/2.]

——, and T. H. Vonder Harr, 1977: Seasonal oceanic precipitation frequencies from Nimbus 5 microwave data. *J. Geophys. Res.*, **82,** 2083–2086.

Kummerow, C., and J. A. Weinman, 1988: Determining microwave brightness temperatures from horizontally finite and vertically structured clouds. *J. Geophys. Res.*, **93,** 3720–3728.

Lee, D. K., and W. P. Byerly, 1981: Improvements to the Nimbus-5 ESMR calibrated brightness temperature data set. Final report on NASA Contract NAS5-25346, System and Applied Sciences Corporation, Riverdale, MD.

Liebmann, B., and D. L. Hartmann, 1982: Interannual variations of outgoing IR associated with tropical circulation changes. *J. Atmos. Sci.*, **39,** 1153–1162.

Lovejoy, S., and G. L. Austin, 1980: The estimation of rain from satellite-borne microwave radiometers. *Quart. J. Roy. Meteor. Soc.*, **106,** 255–276.

Marshall, T. S., and W. M. Palmer, 1948: The distribution of raindrops with size. *J. Meteor.*, **5,** 165–166.

Morrissey, M. L., and J. S. Greene, 1991: The Pacific Atoll Raingage Data Set. Joint Institute for Marine and Atmospheric Research, University of Hawaii, Honolulu, HI, 44 pp.

Oort, A. H., and E. M. Rasmusson, 1971: Atmospheric circulation statistics. NOAA Prof. Pap. 5, U.S. Dept. of Commerce, Rockville, MD.

Prabhakara, C., D. A. Short, W. Wiscombe, and R. S. Fraser, 1986: Rainfall over oceans inferred from Nimbus 7 SMMR: Application to 1982–83 El Niño. *J. Climate Appl. Meteor.*, **25,** 1464–1474.

Quinn, W. H., D. O. Zopf, K. S. Short, and R. K. Yang, 1978: Historical trends and statistics of the southern oscillation, El Niño, and Indonesian droughts. *Fish. Bull.*, **76,** 663–678.

Rao, M. S. V., 1984: Retrieval of worldwide precipitation and allied parameters from satellite microwave observations. *Adv. Geophys.*, **26,** 237–336.

——, W. V. Abbott, and J. S. Theon, 1976: Satellite derived global oceanic rainfall atlas. NASA SP-410, Washington, DC.

Rasmusson, E. M., and T. H. Carpenter, 1982: Variations in tropical sea surface temperature and surface wind fields associated with the Southern Oscillation/El Niño. *Mon. Wea. Rev.*, **111,** 517–528.

——, and J. M. Wallace, 1983: Meteorological aspects of the El Niño/Southern Oscillation. *Science,* **222,** 1195–1202.

Ropelewski, C. F., and M. S. Halpert, 1987: Global and regional scale precipitation patterns associated with the El Niño/Southern Oscillation. *Mon. Wea. Rev.*, **112,** 591–609.

Rosenkranz, P. W., 1982: Inversion of data from diffraction-limited multiwavelength remote sensors. 3. Scanning multichannel microwave radiometer data. *Radio Sci.*, **17,** 257–267.

Sabatini, R. R., and E. S. Merritt, 1973: The Nimbus 5 ESMR and its application to storm detection. Final Report, Contract N62306-72-C0153, EPRF, U.S. Navy, Monterey, California, Earth Satellite Corp., Washington, DC, 45 pp.

Shin, K.-S., P. E. Riba, and G. R. North, 1990: Estimation of area-averaged rainfall over tropical oceans from microwave radiometry: A single channel approach. *J. Appl. Meteor.*, **29,** 1031–1042.

Short, D. A., 1988: Remote sensing of oceanic rainrates by passive microwave sensors: A statistical physical approach. Ph.D. dissertation, Texas A&M University, 86 pp.

——, and G. R. North, 1990: The beam filling error in ESMR-5 observations of GATE rainfall. *J. Geophys. Res.*, **95,** 2187–2194.

Smith, E. A., and S. Q. Kidder, 1978: A multispectral satellite approach to rainfall estimates. Research report, Colorado State University, Fort Collins, CO, 27 pp.

——, and A. Mugnai, 1988: Radiation transfer to space through a precipitation layer at multiple microwave frequencies. Part II. Results and analysis. *J. Climate Appl. Meteor.*, **27,** 1074–1091.

Taljaard, J. J., H. van Loon, H. L. Crutcher, and R. L. Jenne, 1969: Climate of the upper atmosphere. Part I. Southern Hemisphere, Vol. 1. National Center for Atmospheric Research, National Record Center, and Dept. of Defense, Washington, DC.

Theon, J., 1973: A multispectral view of the Gulf of Mexico. *Bull. Amer. Meteor. Soc.*, **54,** 934–937.

Wilheit, T. T., 1972: The electrically scanning microwave radiometer (ESMR) experiment. *The Nimbus-5 User's Guide,* R. R. Sabatini, Ed., NASA Goddard Space Flight Center, 59–104.

——, 1979: A model for the microwave emissivity of the ocean's surface as a function of wind speed. *IEEE Trans. Geosci. Electron.*, **17,** 244–249.

——, J. Theon, W. Shenk, and L. J. Allison, 1973: Meteorological interpretations of the images from Nimbus 5 electrically scanning microwave radiometer. NASA X-651-73-189, Goddard Space Flight Center, 21 pp.

——, M. S. V. Rao, T. C. Chang, E. B. Rodgers, and J. S. Theon, 1975: A satellite technique for quantitatively mapping rainfall rates over the oceans. NASA/GSFC X Doc. 911-75-72.

——, A. T. C. Chang, M. S. V. Rao, E. B. Rodgers, and J. S. Theon, 1977: A satellite technique for quantitatively mapping rainfall rates over the oceans. *J. Appl. Meteor.*, **16,** 551–560.

——, ——, and L. S. Chiu, 1991: Retrieval of monthly rainfall indices from microwave radiometric measurements using probability distribution functions. *J. Atmos. Oceanic. Technol.*, **8,** 118–136.

Wyrtki, K., 1979: The response of sea surface topography to the 1976 El Niño. *J. Phys. Oceanogr.*, **9,** 1223–1231.